Spin Excitations and Flat Electronic Bands in a Kagome Superconductor

A Cr-based kagome system exhibits low-energy magnetic excitations and flat bands close to the Fermi level, suggesting the role of magnetism in its low-temperature emergent properties.

Kagome lattice materials have recently attracted significant attention due to their band structures exhibiting flat bands (FBs) originating from quantum destructive interference of the electronic wave function. In these systems, a tuning of the FB close to the chemical potential can induce electronic instabilities and emergent orders. Extensive experimental studies on kagome lattice materials have shown various types of emergent orders, such as unconventional superconductivity, nematicity, charge density wave (CDW) order, and quantum magnetism. However, these emergent properties have been discussed in relation to characteristic features in the electronic structure, such as Van Hove singularities or Dirac fermions, derived from the inherent topology of the kagome lattice, rather than FBs known in kagome materials. In a major study led by Di-Jing Huang, Qimiao Si, Ming Yi, and Pengcheng Dai, in collaboration with scientists from Taiwan, USA, China, Japan, and Korea, researchers have shown that the low-energy electronic structure of the Cr-based kagome metal superconductor $CsCr_3Sb_5$ is dominated by FBs at the Fermi level (E_F). The researchers observed low-energy magnetic excitations evolving across the low-temperature CDW transition (T_{CDW} = 54 K), suggesting that the low-temperature order has a magnetic origin and that the kagome FBs play a role in the emergence of this order.[1]

The chromium-based kagome metal $CsCr_3Sb_5$ was recently discovered to exhibit a unidirectional CDW order, with superlattice peaks observed by X-ray diffraction (XRD) below T_{CDW} = 54 K. Magnetic susceptibility and nuclear magnetic resonance measurements indicated the simultaneous onset of magnetic order.[2] Band structure calculations revealed multiple competing density wave phases.[3,4] Under hydrostatic pressure, the two orders are separated in temperature and suppressed, and a superconducting dome emerges with a T_C peaking at 6.4 K.[2] Although such a phase diagram resembles those of other unconventional superconducting families, such as the iron-based superconductors and cuprates, the nature of the competing order, as well as evidence of FBs and their association with magnetism across the 54 K CDW phase transition, was not clarified. Using resonant inelastic X-ray scattering (RIXS), angle-resolved photoemission spectroscopy (ARPES), and density functional theory (DFT) calculations, researchers have now shown that the kagome FBs may play an important role in the emergent CDW order.[1]

$CsCr_3Sb_5$ crystallizes in a layered hexagonal lattice consisting of alternatingly stacked Cr–Sb sheets and Cs layers (space group P6/mmm No. 191) with lattice parameters a = 5.4956(1) Å and c = 9.2602(2) Å at 293 K, where the Cr atoms form a kagome lattice (**Fig. 1(a)**).[2] The corresponding 3D BZ is plotted in **Fig. 1(b)**. The authors first characterized the crystal structure at 293 K and then confirmed that superlattice peaks associated with the CDW order set in below T_{CDW}. **Figure 1(c)** shows a map of the reciprocal space in the (H, K, 0) plane where CDW superlattice peaks occurring below T_{CDW} are marked.

The authors carried out RIXS measurements at the Taiwan Photon Source beamline **TPS 41A**. RIXS probes two-particle excitations in momentum transfer q = Δk, such as magnetic excitations, phonons, crystal-field excitations,

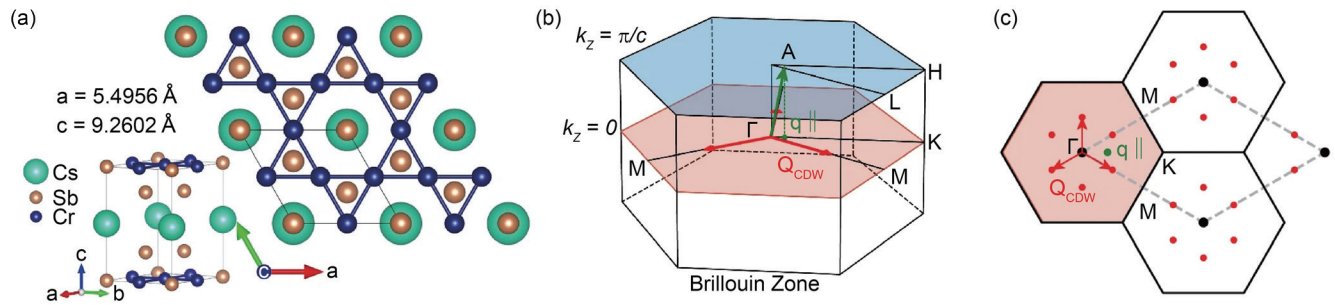

Fig. 1: Crystal structure, Brillouin zone, and CDW order schematics of $CsCr_3Sb_5$. (a) The Cr atoms form a kagome lattice. (b,c) Reciprocal space of $CsCr_3Sb_5$ showing CDW observed by XRD (red arrows or red points). The green arrow marks the q of temperature-dependent RIXS, where q|| is the projection of q onto the sample surface. [Reproduced from Ref. 1]

and plasmons. In particular, it is well-known that magnetic excitations can be conclusively determined when the scattered photons have rotated polarization with respect to the incident beam. **Figure 2(a)** illustrates the scattering geometry of the RIXS experiments carried out by the authors. To conclusively determine spin excitations of the system and exclude other excitations, the authors used π-polarized light with 90° scattering angle between the incident and scattered X-rays of wave vectors k_{in} and k_{out}, respectively. Most importantly, as the dominant low-energy electronic states of $CsCr_3Sb_5$ are derived from Cr 3d orbitals, the authors carried out Cr L_3-edge RIXS to unravel its low-energy excitations. **Figure 2(b)** plots the X-ray absorption spectra across the Cr L_3-edge, and **Fig. 2(c)** plots the RIXS spectra of $CsCr_3Sb_5$ measured at different incident photon energies marked in **Fig. 2(b)**. The 90°-scattering geometry with π-polarized X-rays ensured the measurement of spin excitations and showed a clear spin excitation feature around 70 meV as a shoulder of elastic scattering.

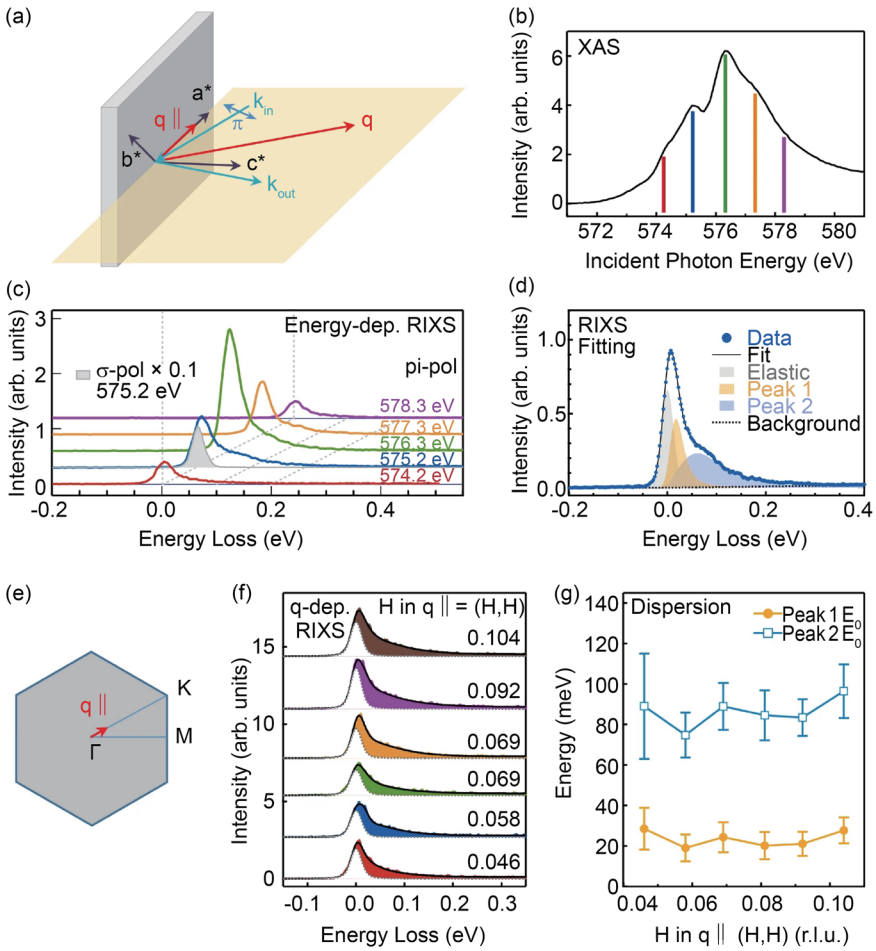

Fig. 2: RIXS measurements. (a) Illustration of RIXS scattering geometry. The scattering plane was perpendicular to the ab plane of $CsCr_3Sb_5$. The incident and scattered wave vectors of X-rays, *i.e.*, k_{in} and k_{out}, are orthogonal. The polarization of incident X-rays was in the scattering plane, *i.e.*, π-polarized, resulting in RIXS with a cross-polarization geometry. The polarization of scattered X-rays was unresolved. The projection of wavevector change q onto the ab plane is denoted as q||. (b) Cr L_3-edge X-ray absorption spectrum of $CsCr_3Sb_5$ recorded at 300 K. Colored vertical bars indicate the X-ray energies used in RIXS measurements. (c) Incident energy–dependent RIXS with q|| along the ΓM direction at 25 K. Spectra in color were recorded with π-polarized X-rays at selected energies. The RIXS spectrum with σ polarization, *i.e.*, X-ray polarization perpendicular to the scattering plane, shows the instrumental energy resolution of RIXS. (d) Curve fitting for measured RIXS spectra was performed using a linear background and a spectral profile consisting of three components: one elastic and two electronic excitations. (e) First Brillouin zone in the a*b* plane of reciprocal space. The red arrow indicates q|| of momentum-dependent RIXS measurements. (f) Momentum-dependent RIXS with q|| along ΓK at 25 K. The energy of incident photons was set to 575.2 eV to optimize the shoulder feature. The dashed lines plot the elastic components; the colored shades indicate spectral profiles arising from spin excitations. (g) Dispersion of fitted undamped energy E_0 of two spin excitations as a function of in-plane momentum q||. [Reproduced from Ref. 1]

The measured RIXS spectrum was fitted to a spectral profile comprising three components: one elastic peak, two electronic excitations, and a polynomial background, as shown in **Fig. 2(d)**. The authors also measured momentum-dependent RIXS with q|| along Γ– K (**Fig. 2(e)**) to further verify that the observed electronic excitations arise from transitions involving FBs. **Figure 2(f)** summarizes the q|| dependence of the magnetic excitations within the available momentum transfer range along the [H, H, 0] direction. The fitted undamped energy E_0 of the two spin components in the RIXS data shows no dispersion for all q|| within the available range, as plotted in **Fig. 2(g)**, indicating direct evidence of FBs. This is consistent with the FB results obtained from ARPES measurements as discussed below.

The authors conducted a comparison of the temperature dependence of the FBs and spin excitations across T_{CDW} using ARPES and RIXS. **Figure 3(a)** shows the ARPES band dispersion map along Γ–M taken with linear vertical (LV) polarization at 10 K (left) and 140 K (right), suitable for selecting the FB of d_{yz} orbital. The FBs are visible at both temperatures, as seen in the map, the peak in the Energy Distribution Curve (EDC) (**Fig. 3(b)**), and the bend in the fitted band dispersion (marked by a white and red arrow, respectively). From the map, the FB location appears closer to E_F at 140 K compared to 10 K. This is seen more clearly in the direct comparison of the EDC (**Figs. 3(b) and 3(c)**) taken at the location marked by the black arrow: the peak is shifted towards E_F at 140 K by about 20 meV, and is recovered after thermally cycling back to

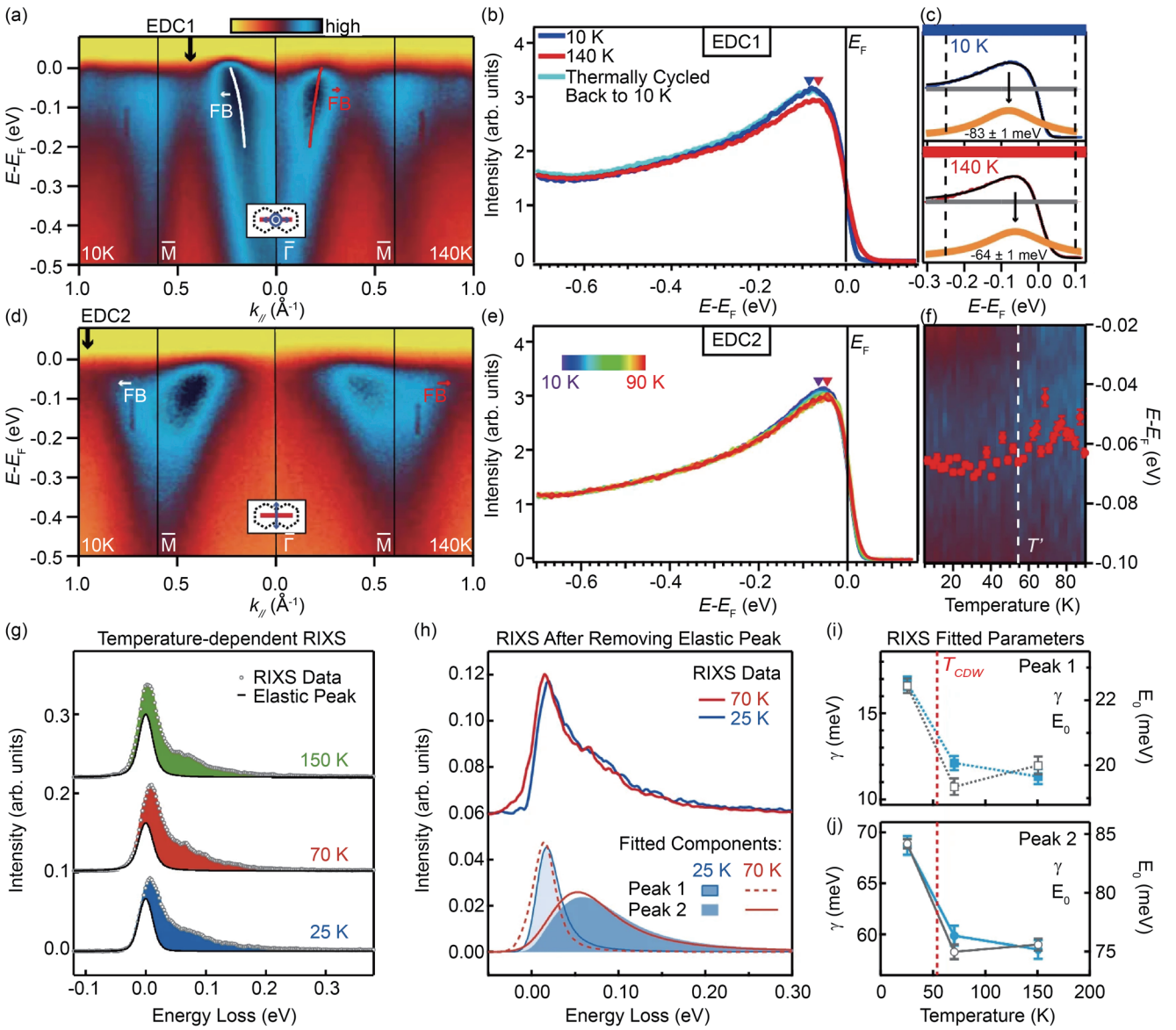

Fig. 3: Temperature-dependent results of ARPES and RIXS. (a) Band dispersion obtained with 114 eV LH polarization and horizontal slit direction at 10 K (left) and 140 K (right). White (10 K) and red (140 K) dots denote the fitted momentum distribution curve positions for the electron pocket at Γ. The arrows mark a kink in the dispersion, indicating hybridization with the FB. (b) EDC1 measured at position marked in (a) at 10 K, 140 K, and thermally cycled back to 10 K. (c) Fitting at 10 K and 140 K for EDC1 showing a Lorentzian peak (orange) with constant background (gray), multiplied by the Fermi–Dirac (FD) function convolved with a Gaussian peak of 40 meV full width at half maximum (FWHM) for experimental resolution. Blue/red dots are the raw data points, the same as (b). Vertical dashed lines mark the fitting range. The dashed arrows denote the fitted Lorentzian peak positions. (d) Same as (a) but measured with LV polarization. (e) EDC2 as marked in (d) measured from 10 K to 90 K. (f) Fitted FB positions from EDCs after dividing the FD function convolved with a Gaussian peak with 40 meV FWHM. The dotted line marks the transition T_{CDW}. (g) Temperature-dependent RIXS. Open circles depict raw RIXS data measured with π-polarized incident X-rays at an energy of 572.5 eV and temperatures of 25, 70, and 150 K; solid lines plot the fitted elastic components. The shaded areas denote RIXS features arising from spin excitations. (h) RIXS spectra at 25 K (blue) and 70 K (red) after removing the elastic component. The bottom panel compares the fitted components of spin excitations. (i,j) Evolution of fitted parameters E_0 and γ for temperatures across T_{CDW} (vertical dashed line). [Reproduced from Ref. 1]

10 K. Similarly, the comparison of band dispersion along Γ–M taken with linear horizontal (LH) polarization and horizontal slit at 10 K ($T < T_{CDW}$) and 140 K ($T > T_{CDW}$) shows that FB of d_{xz} orbital also shift towards E_F (**Figs. 3(d) and 3(e)**). The authors plotted the continuous temperature evolution of this shift, as presented in **Fig. 3(f)**. They also conducted temperature-dependent RIXS measurements at temperatures across T_{CDW}. **Figure 3(g)** presents the measured RIXS spectra within an energy range of 0.3 eV. All spectra were analyzed using the same curve-fitting scheme as shown in **Fig. 2(d)**. To highlight the spectral changes, **Fig. 3(h)** compares RIXS spectra above and below T_{CDW} after removing elastic scattering, revealing a subtle but distinct broadening and shift toward higher energy as the temperature is cooled across T_{CDW}. For quantitative analysis, **Figs. 3(i) and 3(j)** show the evolution of the fitted bare energy E_0 and damping factor γ of both spin excitations, consistent with ARPES results shown in **Fig. 3(f)**.[4] The observed excitations are coupled to the electron–hole excitations across E_F. Thus, the broadening and shifting of

the spin excitations likely reflect the shifting of the FBs away from E_F, both below and above E_F.[1]

Finally, the authors discuss that while their bare DFT electronic structure calculations do not accurately reproduce the observed bands below E_F, but when the necessary correlation corrections reconciles the discrepancies in the FB position at a qualitative level. This confirms the potential mechanism for the involvement of the kagome FBs in the formation of the CDW electronic order. Furthermore, since the chemical potential of $CsCr_3Sb_5$ is close to the kagome FBs, it is conceivable that their presence drives an electronic order that pushes the FBs away from the E_F, as observed in experiments. With hydrostatic pressure, this electronic CDW order can get suppressed and leave residual density of states from the FBs near E_F to experience the quantum fluctuations expected near a quantum critical point and potentially enable superconductivity. The authors conclude that the flat band in $CsCr_3Sb_5$ is clearly participates in the low-temperature order, as is evident from its shift away from E_F and its coupling with spin excitations.[1] (Reported by Ashish Chainani)

This report features the work of Di-Jing Huang, Qimiao Si, Ming Yi, Pengcheng Dai and their collaborators published in Nat. Commun. ***16****, 7573 (2025).*

TPS 41A Soft X-ray Scattering

- RIXS
- Materials Science, Condensed-matter Physics

References

1. Z. Wang, Y. Guo, H.-Y. Huang, F. Xie, Y. Huang, B. Gao, J. S. Oh, H. Wu, J. Okamoto, G. Channagowdra, C.-T. Chen, F. Ye, X. Lu, Z. Liu, Z. Ren, Y. Fang, Y. Wang, A. Biswas, Y. Zhang, Z. Yue, C. Hu, C. Jozwiak, A. Bostwick, E. Rotenberg, M. Hashimoto, D. Lu, J. Kono, J.-H. Chu, B. I. Yakobson, R. J. Birgeneau, G.-H. Cao, A. Fujimori, D.-J. Huang, Q. Si, M. Yi, P. Dai, Spin excitations and at electronic bands in a Cr-based kagome superconductor, Nat. Commun. **16**, 7573 (2025).
2. Y. Liu, Z.-Y. Liu, J.-K. Bao, P.-T. Yang, L.-W. Ji, S.-Q. Wu, Q.-X. Shen, J. Luo, J. Yang, J.-Y. Liu, C.-C. Xu, W.-Z. Yang, W.-L. Chai, J.-Y. Lu, C.-C. Liu, B.-S. Wang, H. Jiang, Q. Tao, Z. Ren, X.-F. Xu, C. Cao, Z.-A. Xu, R. Zhou, J.-G. Cheng, G.-H. Cao, Nature **632**, 1032 (2024).
3. C. Xu, S. Wu, G.-X. Zhi, G. Cao, J. Dai, C. Cao, X. Wang, H.-Q. Lin, Nat. Commun. **16**, 3114 (2025).
4. S. Wu, C. Xu, X. Wang, H.-Q. Lin, C. Cao, G.-H. Cao, Nat. Commun. **16**, 1375 (2025).

How Antiferromagnetism Shapes Superconductivity in Cuprate Materials

Their remarkable work links hidden magnetism to the birth of superconductivity in complex quantum materials.

Superconductivity in cuprates has remained a central challenge for more than four decades. Despite the discovery of numerous competing and intertwined phases, one of the most robust and universal features of the cuprate phase diagram is the dome-shaped T_C that arises near the boundary of antiferromagnetic (AF) order. This proximity has long suggested that AF spin fluctuations may serve as the pairing mechanism for superconductivity. Theoretical studies have explained the unconventional d-wave pairing symmetry within this framework, while angle-resolved photoemission spectroscopy (ARPES) has provided direct experimental access to quasiparticles and their many-body renormalization effects. However, determining how AF spin fluctuations specifically affect electronic states and promote superconductivity remains challenging due to strong correlations and the complexity of the cuprate phase diagram.

In the presence of long-range AF order at low electron doping, a superlattice potential folds the electronic bands and reconstructs the Fermi surface from a large hole-like cylinder into smaller electron and hole pockets. While this folding is well understood within mean-field descriptions of long-range AF order, remnants of reconstructed pockets have also been observed in the superconducting regime beyond the long-range AF phase boundary. These observations suggest a role for short-range AF fluctuations or other ordering phenomena. Further complicating the interpretation, ARPES studies have reported the simultaneous presence of both folded AF bands and unfolded pristine bands, indicating strong electron correlations and challenging conventional models.